

Controlling Structure and Morphology of MoS₂ via Sulfur Precursor for Optimized Pseudocapacitive Lithium Intercalation Hosts

Maciej Tobis,^[a, b, c] Mennatalla Elmanzalawy,^[b, c] Jaehoon Choi,^[b, c] Elżbieta Frąckowiak,^{*[a]} and Simon Fleischmann^{*[b, c]}

Molybdenum disulfide (MoS₂)-based electrode materials can exhibit a pseudocapacitive charge storage mechanism induced by nanosized dimension of the crystalline domains, which is why control over material structure via synthesis conditions is of significance. In this study, we investigate how the use of different sulfide precursors, specifically thiourea (TU), thioacetamide (TAA), and L-cysteine (LC), during the hydrothermal synthesis of MoS₂, affects its physicochemical, and consequently, electrochemical properties. The three materials obtained exhibit distinct morphologies, ranging from micron-sized architectures (MoS₂ TU), to nanosized flakes (MoS₂ TAA and LC).

While all three synthesized samples exhibit pseudocapacitive Li⁺ intercalation properties, the capacity retention of the latter two consisting of nanosized flakes is further improved at high cycling rates. The individual charge storage properties are analyzed by operando X-ray diffraction, dilatometry, and 3D Bode analysis, revealing a correlation between the morphology, porosity, and the electrochemical intercalation behavior of the obtained electrode materials. The results demonstrate a facile strategy to control MoS₂ structure and related functionality by choice of hydrothermal synthesis precursors.

Introduction

Molybdenum disulfide (MoS₂) is among the most studied transition metal dichalcogenides, a family of materials characterized by their two-dimensional character with individual layers stacked by van der Waals forces.^[1] MoS₂ has gained attention due to its applicability in a wide range of fields like electrochemical energy storage^[2,3] and electrocatalysis.^[4,5] There are several polytypes of MoS₂, with the naturally occurring, semiconducting 2H-MoS₂ and 3R-MoS₂ polytypes, and the synthetically accessible, metallic 1T-MoS₂.^[6] The functional properties of MoS₂ are highly dependent on the polytype, as well as on the morphology and crystallite size of the material, which is why synthesis strategies able to control these properties are required.^[7,8]

In the field of electrochemical energy storage, MoS₂ has been employed as an anode material suitable for lithium and sodium ion storage, with the possibility to store charge via

electrochemical intercalation and/or conversion reactions, depending on the utilized voltage window.^[9–12] When used as an intercalation host, it was found that kinetically favorable intercalation properties are obtained when MoS₂ crystallite size is reduced.^[13] For such nanosized MoS₂, Cook et al. report the emergence of solid-solution intercalation with pseudocapacitive properties, that is, Faradaic charge storage with a capacitor-like signature over a wide voltage range in absence of kinetic diffusion limitations.^[13,14] It was also found that the introduction of crystal defects, as well as the increase of the MoS₂ d-spacing via hexanediamine pillars amplifies the pseudocapacitive electrochemical lithiation response.^[15,16] For 2H-MoS₂, an irreversible transition to 1T-MoS₂ during the first electrochemical lithiation cycle at around 1.1 V vs. Li⁺/Li leads to an unfavorably low initial Coulombic efficiency.^[17] The findings underline the significance of controlling MoS₂ crystal structure, crystallite size, and morphology, to obtain desired functional properties.

Not only electrochemical charge storage, but also the electrocatalytic hydrogen evolution (HER) performance is dependent on MoS₂ crystal structure and morphology.^[18] This led to the exploration of various hydrothermal synthesis routes controlling MoS₂ structure by choice of sulfur-precursor.^[19–22] Liu et al. found that thioacetamide (TAA) and L-cysteine (LC) possess lower decomposition temperatures than thiourea (TU), thereby releasing sulfur more readily, leading to smaller particle sizes and the tendency to form the 1T-polytype, which in turn, leads to a favorable HER activity.^[23]

The findings motivated us to explore the impact of sulfur precursors on the electrochemical lithium intercalation performance of hydrothermally synthesized MoS₂ materials. Given the relative ease and scalability of hydrothermal synthesis over synthesis routes like vapor deposition or thermal conversion of

[a] M. Tobis, E. Frąckowiak
Poznan University of Technology (PUT), Poznań 60965, Poland
E-mail: elzbieta.frackowiak@put.poznan.pl

[b] M. Tobis, M. Elmanzalawy, J. Choi, S. Fleischmann
Helmholtz Institute Ulm (HIU), Ulm 89081, Germany

[c] M. Tobis, M. Elmanzalawy, J. Choi, S. Fleischmann
Karlsruhe Institute of Technology (KIT), Karlsruhe 76021, Germany
E-mail: simon.fleischmann@kit.edu

Supporting information for this article is available on the WWW under <https://doi.org/10.1002/batt.202400277>

© 2024 The Authors. *Batteries & Supercaps* published by Wiley-VCH GmbH. This is an open access article under the terms of the Creative Commons Attribution License, which permits use, distribution and reproduction in any medium, provided the original work is properly cited.

molybdenum oxides in sulfidizing atmospheres, gaining better understanding of the relation between hydrothermal synthesis route, MoS₂ microstructure and the electrochemical performance are crucial to further develop MoS₂ as a promising electrode material in (pseudocapacitive) ion intercalation hosts.

In this study, we highlight the role of sulfur precursor selection in the hydrothermal synthesis of MoS₂ materials, showing its profound influence on their final structural, morphological, and porous texture characteristics. The choice of the precursor dictates the morphology of MoS₂ with secondary particle size ranging from micro- to nano-sized dimensions, consequently impacting the available interfacial area. The resulting physicochemical properties of the synthesized MoS₂ are linked with their electrochemical response, revealing emergence of pseudocapacitive intercalation phenomena upon nanostructuring. Lithiation kinetics of MoS₂ with improved values of capacity at higher currents are linked with greater electrode/electrolyte interface area. Comprehensive analyses, employing techniques such as *operando* XRD, 3D Bode plot analysis, and dilatometric studies reveal solid-solution charge storage mechanism induced by the nanostructured particle size dimensions and different electrode volume change upon de/lithiation. The insights of the study can guide synthesis development of MoS₂-based materials for application in electrochemical energy storage, conversion, and beyond.

Experimental Section

Materials Synthesis

Different nanostructured molybdenum disulfides (MoS₂) were prepared during separate hydrothermal reactions using 1.6 g of sulfur source, i.e., thiourea (Sigma Aldrich, 99%), thioacetamide (Sigma Aldrich, 99%), or L-cysteine (Sigma Aldrich, 97%) and 1.6 g of sodium molybdate (Sigma Aldrich, 98%). Both precursors were dissolved together in 160 ml of deionized water and the pH of the solution was adjusted to 7 with the use of 1 M hydrochloric acid (POCH S.A.). Hydrothermal syntheses were conducted in hydrothermal reactor (Parr 5500 HP) with stirring at 200 rpm during 24 h at 200 °C with 20 bar of internal pressure. After the reaction, black precipitate was collected through vacuum filtration and washing with aliquots of deionized water and ethanol. Powder materials were dried at 80 °C overnight. Micrometric-sized MoS₂ was purchased from Sigma-Aldrich (particle size below 2 μm, 99%).

Physicochemical Characterization

A Crossbeam x340 (Zeiss) scanning electron microscope (SEM) was used to analyze the morphology of the samples at different magnifications using 5 kV acceleration voltage. Transmission electron microscopy (TEM) analysis was performed using a Talos F200i microscope (Thermo Fisher Scientific) operating at 80 kV. Samples were prepared through sonication in ethanol and deposition on a lacey carbon-coated copper TEM grid by drop-casting. Powder X-ray diffraction (XRD) patterns of the MoS₂ materials were obtained by using a Bruker D8 Advance diffractometer operating in Bragg-Brentano geometry with a Cu Kα radiation source ($\lambda = 1.5406 \text{ \AA}$). Raman spectroscopy measurements were obtained by using a Renishaw InVia confocal Raman microscope with a 532 nm laser at a low power of 100 μW. Sorption isotherms of N₂ at 77 K were

recorded with the use of ASAP 2460 (Micromeritics, USA). The materials were degassed in a flow of helium at 100 °C for 12 h. Prior the N₂ sorption, the samples were degassed in vacuum for 6 h. Brunauer-Emmett Teller (BET) model was utilized to evaluate the specific surface area (SSA) using 0.01 to 0.05 P/P₀ range. The elemental composition of prepared samples was evaluated by using Thermo Fisher Scientific FlashSmart Elemental Analyzer. The elemental content of C, H, N, S was estimated in the column filled with copper and copper (II) oxide during incineration at 950 °C. Separate pyrolysis of samples at 1060 °C in a column filled with nickel coated carbon was used to estimate the content of O.

Electrochemical Cell Setup and Characterization

Electrode Preparation

Electrode slurries consisted of 80 wt.% of active material, 10 wt.% of conductive agent (C65, C-NERGY), and 10 wt.% of binder (polyvinylidene fluoride, PVDF, Solvay) dispersed in a N-Methyl-2-pyrrolidone (NMP, Thermo Scientific). Prior to the mixing, powder components were ground in a mortar to uniform the particles. All constituents were added to a plastic container and transferred to a speed mixer (ARE-250, Thinky) and mixed for 10 min at 10.000 rpm. Electrode slurries were later cast on carbon-coated aluminum foils with a wet thickness of about 60 μm by using a doctor blade. Wet films were dried at 80 °C overnight, followed by punching circular electrodes with a diameter of 12 mm. Such prepared electrodes were further dried at 80 °C under vacuum overnight before being transferred to an argon filled glovebox (MBraun, H₂O and O₂ content below 1 ppm).

Electrochemical Studies

Electrochemical behavior of prepared electrodes was examined in a coin cell (CR2032, Hohsen Corp.) configuration employing 14 mm lithium metal disc (Honjo) as the negative electrode separated by a porous membrane (GF/A, Whatman) soaked with 200 μL of LP30 electrolyte (1 M LiPF₆ in a 1:1 vol.% mixture of ethylene carbonate/dimethyl carbonate (EC:DMC)). Assembled coin cells were studied by cyclic voltammetry at different sweep rates (from 0.2 to 20 mV s⁻¹), where the measured current is normalized by the active material mass and the sweep rate, resulting in the unit of A s (V g)⁻¹, allowing for easier estimation of the stored charge at various sweep rates, and galvanostatic charge/discharge at different specific currents (20 mA g⁻¹ to 10 A g⁻¹) between 3–1 V vs. Li/Li⁺. Staircase potential-electrochemical impedance spectroscopy (SPEIS) was performed in a frequency range between 1 MHz and 10 mHz in 20 steps, i.e., 100 mV increments between 3 to 1 V vs. Li/Li⁺, with 10 min chronoamperometric steps between potential increments before each EIS measurement. The impedance was analyzed according to prior work,^[24] with the real capacitance being calculated according to equation (1):

$$C'(\omega) = -\frac{Z''(\omega)}{\omega|Z(\omega)|^2 m} \quad (1)$$

where $C'(\omega)$ is the real part of the capacitance, $Z''(\omega)$ the imaginary part of the impedance, ω the angular frequency ($\omega = 2\pi f$, with f as the frequency), $|Z(\omega)|$ is the magnitude of the impedance, and m the electrode active mass. All the electrochemical measurements were performed through a multichannel potentiostat/galvanostat (VMP3, Biologic)

Electrochemical Operando XRD Measurements

Electrode slurries for operando XRD measurements were prepared as described above, but with a weight ratio of active material to conductive carbon to binder of 7:2:1 in order to ensure sufficient electric conductivity throughout the thicker coating. The slurry was then drop-cast onto Ti mesh, with mass loading of ca. 5 mg cm⁻², and left to dry under air circulation, then later under vacuum at 80°C. Operando XRD patterns were recorded during galvanostatic cycling of the electrodes against Li metal in LP30 electrolyte with a specific current of 50 mA g⁻¹, in a modified coin cell setup with thin Kapton windows on both sides of the coin cell. The diffractograms were obtained using a STOE STADI-p diffractometer in Debye-Scherrer geometry with Mo K α radiation source ($\lambda=0.70932\text{ \AA}$), equipped with a MYTHEN 1 K detector and a STOE coin cell holder. The electrochemical measurements were performed using a potentiostat (SP-300, Biologic).

Electrochemical Operando Dilatometry Measurements

For dilatometry studies, selected electrode materials were prepared in form of self-standing electrodes containing 80 wt.% of active material, 10 wt.% of conductive carbon (C65, C-NERGY), and 10 wt.% of binder (polytetrafluoroethylene – PTFE, 60 wt.% dispersion in water, Sigma Aldrich). Constituents were mixed in 20 ml of isopropanol, grounded in a mortar and mixed until isopropanol has evaporated. After a dough-like consistency has been formed, the material was calendered to obtain a sheet of material with uniform thickness. The sheet was cut into 8 mm diameter discs and subsequently dried at 80°C overnight under vacuum. Before transferring the electrodes inside the glovebox, the thickness of each electrode was measured (ca. 60 μm). Operando electrochemical dilatometry experiments were performed by using ECD-3-nano electrochemical dilatometer (EL-Cell). The working electrode was separated by a stiff glass frit and a porous membrane (GF/A, Whatman) from a 10 mm lithium disc (Honjo). After assembly, the cell was maintained at OCV for period of 6 h to obtain a stable electrode height measurement. The electrode height change is expressed in a form of percentage calculated from the first measurements. The electrochemically-induced height-changes were evaluated with the dilatometer during galvanostatic charge/discharge at 20 mA g⁻¹ between 3 to 1 V vs. Li/Li⁺. Electrochemical experiments were performed with a multichannel potentiostat/galvanostat (VMP3, Biologic).

Results and Discussion

Physicochemical Characterization

Different MoS₂ materials are synthesized from various sulfur precursors, namely thiourea (TU), thioacetamide (TAA), and L-cysteine (LC), by a hydrothermal approach at the same temperature, time, pH of the solution and precursor mass (Figure 1A).

Scanning electron microscopy (SEM) shows that dependent on the type of the precursor, different surface morphologies are obtained (Figure 1B–E). Commercially available MoS₂ (Comm) (Figure 1B) utilized for comparison presents micrometer-sized secondary particles consisting of primary flakes with layered features shown at higher magnifications. In contrast, materials obtained via hydrothermal reactions show different morphologies and particle size distributions dependent on the type of precursor. MoS₂ obtained from TU (Figure 1C) shows tens of microns large structures with bump-like surface features, on which nanosized, perpendicularly oriented flakes are visible. In sharp contrast, MoS₂ obtained from TAA (Figure 1D) and from LC (Figure 1E) show 0.5–1 micron-sized secondary particle agglomerates consisting of smaller, below 100 nm sized primary particles. They follow a similar trend as previous reports, with MoS₂ derived from TU precursor yielding the largest secondary particle sizes.^[23] The observed differences of the samples show a high dependence of resulting macroscopic MoS₂ structure and morphology from the sulfur precursor employed in the hydrothermal synthesis.

The purity of hydrothermally synthesized samples is analyzed in terms of their elemental composition (Table 1) showing comparable formulation to MoS₂ Comm. Often, hydrothermal preparation of MoS₂ using organic precursors leads to formation of some amorphous carbon impurities.^[25] In this case, each material shows low content of carbon in comparable quantity to MoS₂ Comm. Lack of nitrogen content in MoS₂ TAA and MoS₂ LC suggests the absence of unreacted precursor residue in the samples, whereas MoS₂ TU shows a small quantity of nitrogen (1.6 wt.%), which was previously reported to increase the interlayer distance of MoS₂.^[26] The findings show correlation between the lower decomposition temperatures of TAA and LC compared to TU and the resulting nitrogen impurity content. MoS₂ samples derived from TU and LC show some oxygen residue (ca. 4 wt.%), which can be a consequence of the relatively high precursor decomposition temperature (TU) and/or the high oxygen content of the precursor (LC). The analysis reveals that purity of hydrothermally synthesized MoS₂ samples can be affected to some extent by the choice of sulfur precursor. The impact of impurities on the electrical conductivity of resulting electrodes is investigated by 4-point probe method (Table S1), but no correlation is found. Instead, electrode electrical conductivity can be correlated with particle size (vide infra), with higher electrode conductivity for larger particle sizes.

Investigation of the crystal structure of the formed samples is carried out by powder X-ray diffraction (XRD), presented in Figure 2A. MoS₂ Comm shows sharp and well-defined diffrac-

Table 1. Elemental composition of prepared materials from CHNSO analysis.

Sample	C (wt.%)	H (wt.%)	N (wt.%)	S (wt.%)	O (wt.%)	Sum (wt.%)
MoS ₂ Comm	1.3	0.2	0.0	51.8	0.1	53.4
MoS ₂ TU	1.3	0.7	1.6	48.4	3.9	55.8
MoS ₂ TAA	0.9	0.3	0.0	52.4	0.8	54.3
MoS ₂ LC	2.0	0.5	0.0	46.7	3.8	53.0

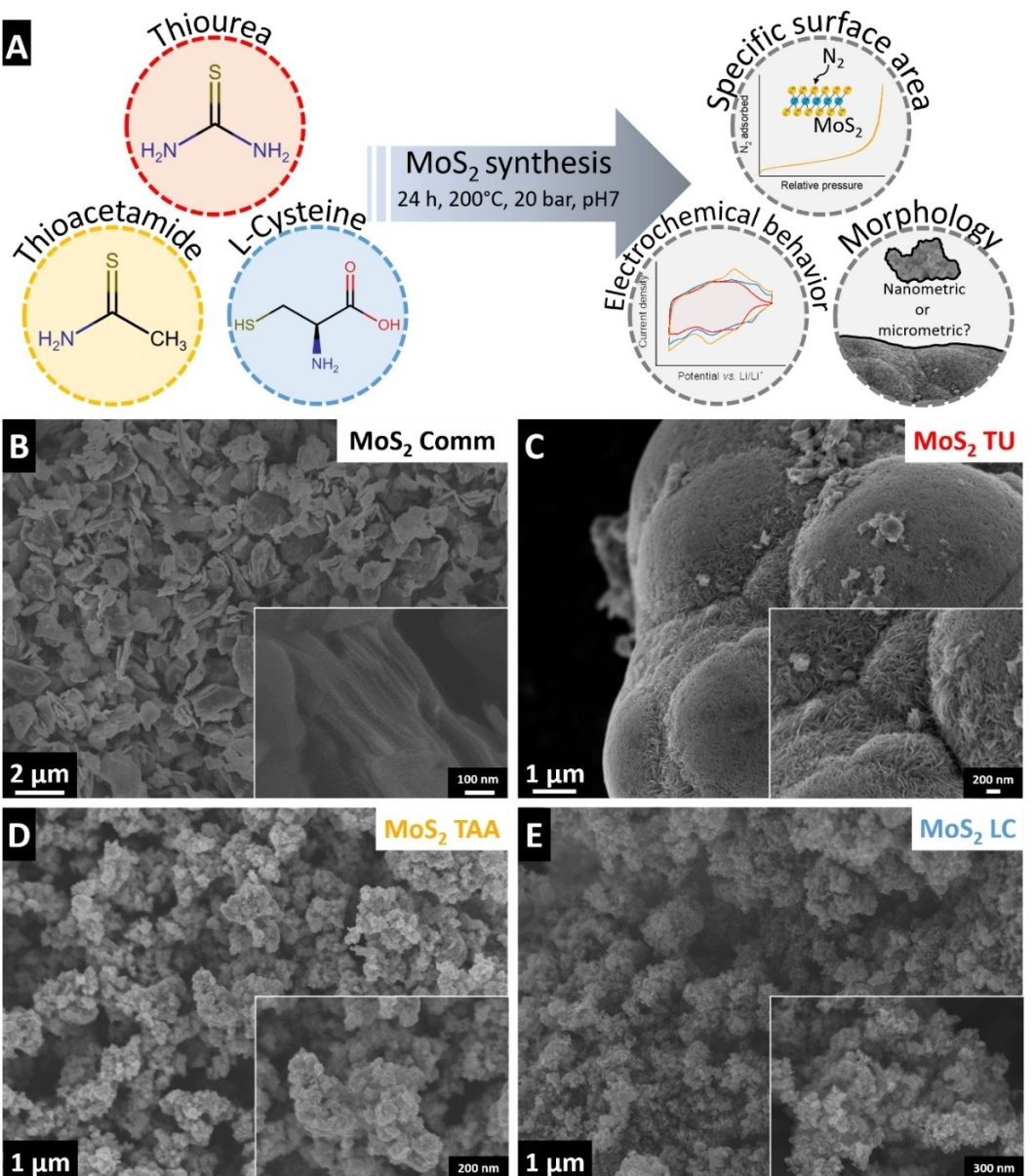


Figure 1. (A) Schematic illustration of the hydrothermal synthesis of MoS₂ materials from different precursors. Scanning electron micrographs of (B) MoS₂ Comm, (C) MoS₂ TU, (D) MoS₂ TAA, and (E) MoS₂ LC.

tion peaks corresponding to the crystallographic planes of hexagonal MoS₂ (2H) indexed by ICDD PDF card no. #01-071-9809. Sharp, high intensity diffraction signals indicate large crystallite sizes of MoS₂ Comm. In contrast, hydrothermally prepared MoS₂ samples display broadening of the diffraction peaks indicating reduced crystallite sizes and/or increased structural disorder compared to MoS₂ Comm. The position of the (002) diffraction signal corresponding to the interlayer distance varies depending on the utilized sulfur precursor, with maxima of the broad signals between 2θ values of ca. 11.9–13.7°, indicative of average interlayer spacings of the obtained MoS₂ materials between ca. 0.64–0.75 nm, which is above that of commercial MoS₂ Comm at 0.61 nm. The irregular, slightly expanded interlayer spacing measured by XRD does not

correlate with the impurity content, since MoS₂ TAA as the sample with most deviation of the interlayer distance from MoS₂ Comm contains least impurities (Table 1). Therefore, the expanded interlayer spacing may be a result of partial water adsorption between the MoS₂ layers, as was observed previously for TAA-derived MoS₂.^[23] Diffraction peaks corresponding to the (100), (103), and (110) sets of planes are in comparable position to MoS₂ Comm, indicating that lattice parameter modification resulting from hydrothermal synthesis is mostly limited to the interlayer spacing.

Figure 2 shows Raman spectra for samples in two different regions corresponding to the 1T (J_1 , J_2 , J_3 modes) and 2H phases (A_{1g} , E_{1g} and E_{2g} modes) of MoS₂, respectively. In case of MoS₂ Comm, distinct peaks positioned at 407 cm⁻¹, 381 cm⁻¹, and

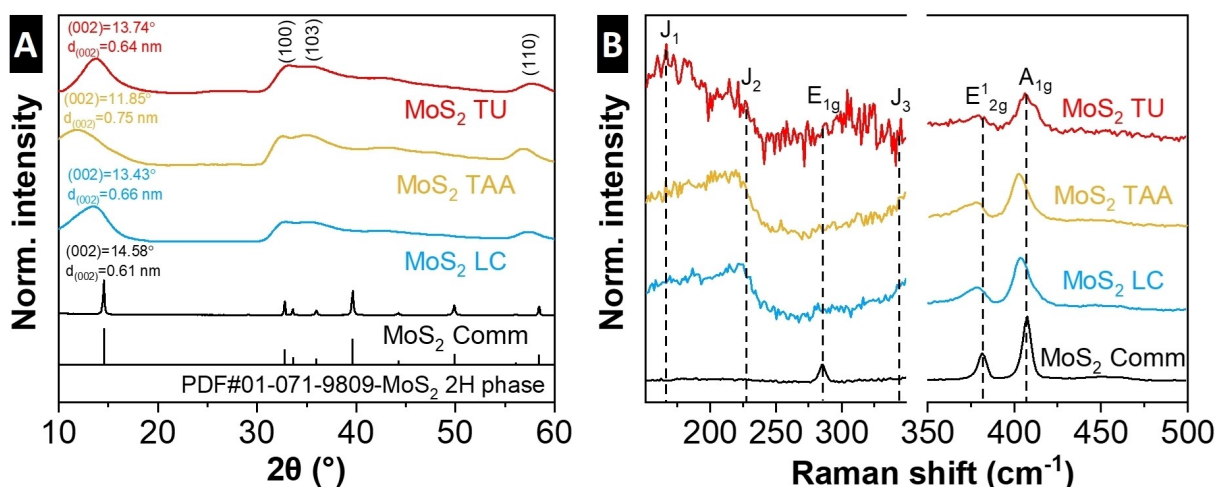


Figure 2. Physicochemical characterization of MoS_2 -based materials. (A) X-ray diffraction patterns and (B) Raman characterization of MoS_2 in 1T and 2H phase regions. In the 1T region ($< 350 \text{ cm}^{-1}$), the intensity is multiplied by a factor of 8 for clarity.

284 cm^{-1} can be assigned to the A_{1g} , E^1_{2g} and E_{1g} modes which are consistent with the characteristic vibrational and stretching modes of 2H phase.^[27] Their presence and position are a confirmation of well-defined crystalline domains. Raman spectra of hydrothermally synthesized MoS_2 samples also show the presence of E^1_{2g} and A_{1g} modes, confirming the presence of 2H- MoS_2 in these samples. However, peak broadening and shifting can be observed, specifically for MoS_2 TAA and MoS_2 LC samples. Typically, Raman analysis shows strong relationship between the number of successive layers in the MoS_2 crystallites and position of the A_{1g} and E^1_{2g} modes.^[27] Shifts of the peaks are commonly observed when increasing the number of adjacent layers in the crystal unit starting from mono to multilayer (from 385 to 381 cm^{-1} for E^1_{2g} and from 403 to 407 cm^{-1} for A_{1g}).^[28] A_{1g} mode corresponding to out-of-plane S atoms vibrations for MoS_2 TAA and LC is positioned at 385 cm^{-1} , which suggests multilayer MoS_2 , whereas the position of the E^1_{2g} shifts to 403 cm^{-1} suggesting MoS_2 monolayer. Such effect could be the result of the nanostructuring of the MoS_2 TAA and LC crystallites. No shift of A_{1g} mode is observable for MoS_2 TU, showing comparable peak positions to MoS_2 Comm possibly related to the micron-sized particles. At the same time, peaks positioned at 226 cm^{-1} corresponding to the J_2 mode suggest the simultaneous existence of the 1T phase in the hydrothermally synthesized samples. This is in agreement with other works on hydrothermally synthesized MoS_2 .^[29,30]

Using transmission electron microscopy (TEM) analysis, morphological and crystallographic properties of the hydrothermally synthesized MoS_2 samples are studied at a nanoscale. Morphological features are shown in TEM (Figure 3A, C, E), where all samples exhibit relatively small crystallites with only few MoS_2 layers (in line with broad (002) signal from XRD). The directly measured interlayer distances are closer to the value of ideal 2H- MoS_2 of 0.61 nm ($\pm 0.03 \text{ nm}$) for all samples than suggested by the XRD results, which may be a result of volatile interlayer species removal (such as interlayer water) in the microscope (ultra-high vacuum and high-energy electron beam

conditions). Utilizing selected area electron diffraction (SAED, Figure 3B, D, F), broad diffraction rings corresponding to the (100) and (110) MoS_2 planes are observed with only small differences of the average lattice parameters between the samples. Overall, TEM investigation reveals that on a nanoscopic level, the crystallite size and shape of MoS_2 domains are more comparable, whereas on a macroscopic level observed by SEM, particle size and/or shape showed stronger differences between these samples.

Nitrogen sorption is conducted to evaluate the porosity and specific surface area (SSA) of the MoS_2 samples. Sorption isotherms of all samples exhibit a type II shape according to IUPAC classification (Figure 4), typically ascribed to nonporous or macroporous samples.^[31] For MoS_2 TAA, MoS_2 LC and MoS_2 TU samples, the emergence of H3-type hysteresis loops confirms the presence of aggregated plate-like particles (Figure 4B-D), as already observed in electron micrographs. However, hysteresis loop for MoS_2 TU (Figure 4B) shows a much steeper desorption branch in comparison to the other two samples, reminiscent of H2(a) loops where the behavior is ascribed to blocked pores and/or narrow pore necks,^[31] which could be formed within the micron-sized secondary particles of MoS_2 TU. This strongly suggests significantly hindered accessibility of pores within the large particles of TU-derived MoS_2 exhibiting a different morphology than MoS_2 TAA and MoS_2 LC despite similar hydrothermal synthesis parameters and despite similarly small crystalline domain sizes observed from TEM and from broadened XRD peaks. The observations are further reflected in the different specific surface areas derived from BET method (Brunauer-Emmett-Teller, ref.^[32]), ranging from relatively small SSA of 8 and $5 \text{ m}^2 \text{ g}^{-1}$ for MoS_2 Comm and MoS_2 TU, to larger SSA of 84 and $34 \text{ m}^2 \text{ g}^{-1}$ for MoS_2 TAA and MoS_2 LC, respectively. The results underline the possibility to tune both porosity and SSA of hydrothermally synthesized MoS_2 via choice of sulfur precursor, which can have significant implications on the materials' functional properties.^[16]

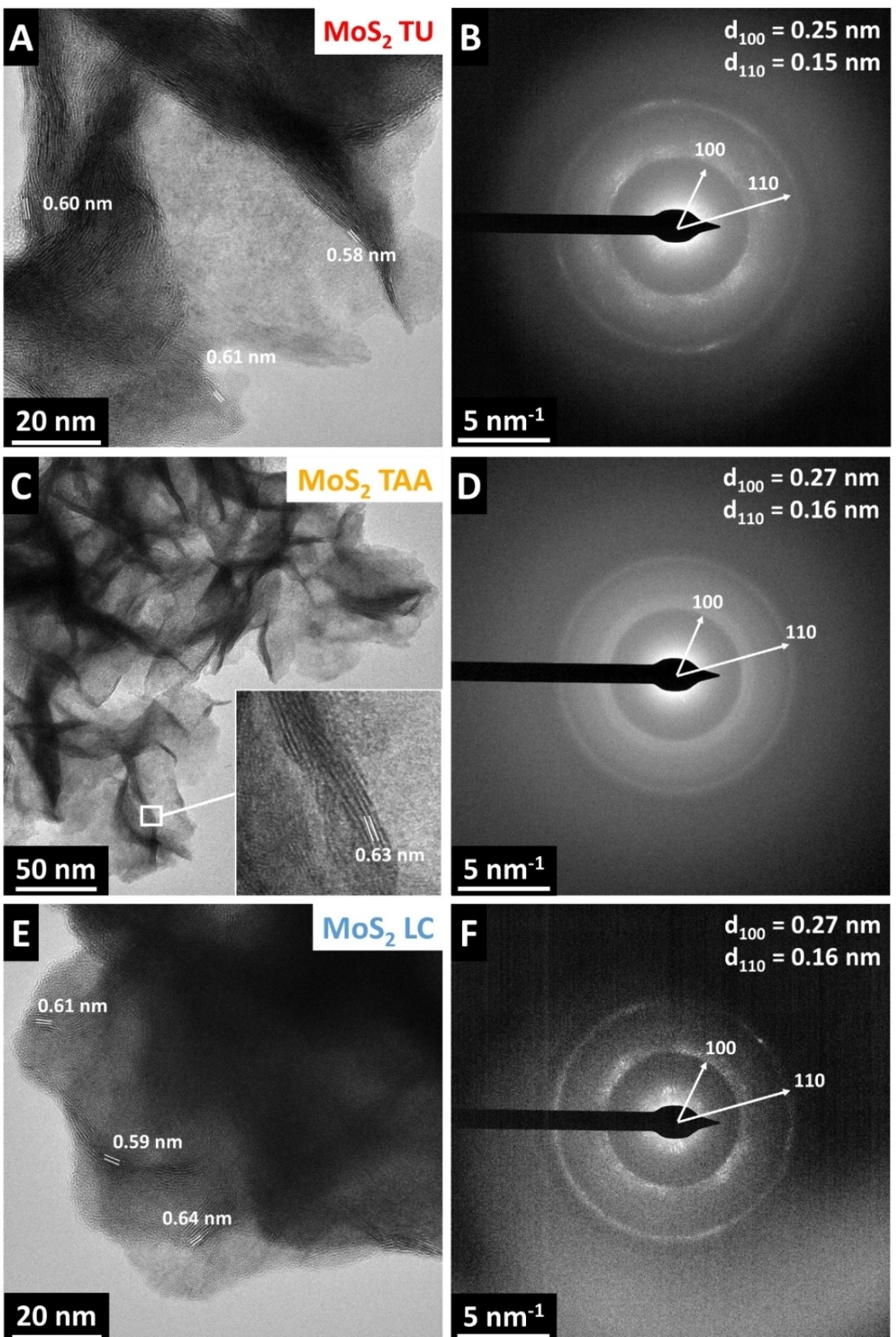


Figure 3. TEM images and corresponding selected area electron diffraction patterns of (A–B) MoS_2 TU, (C–D) MoS_2 TAA, and (E–F) MoS_2 LC.

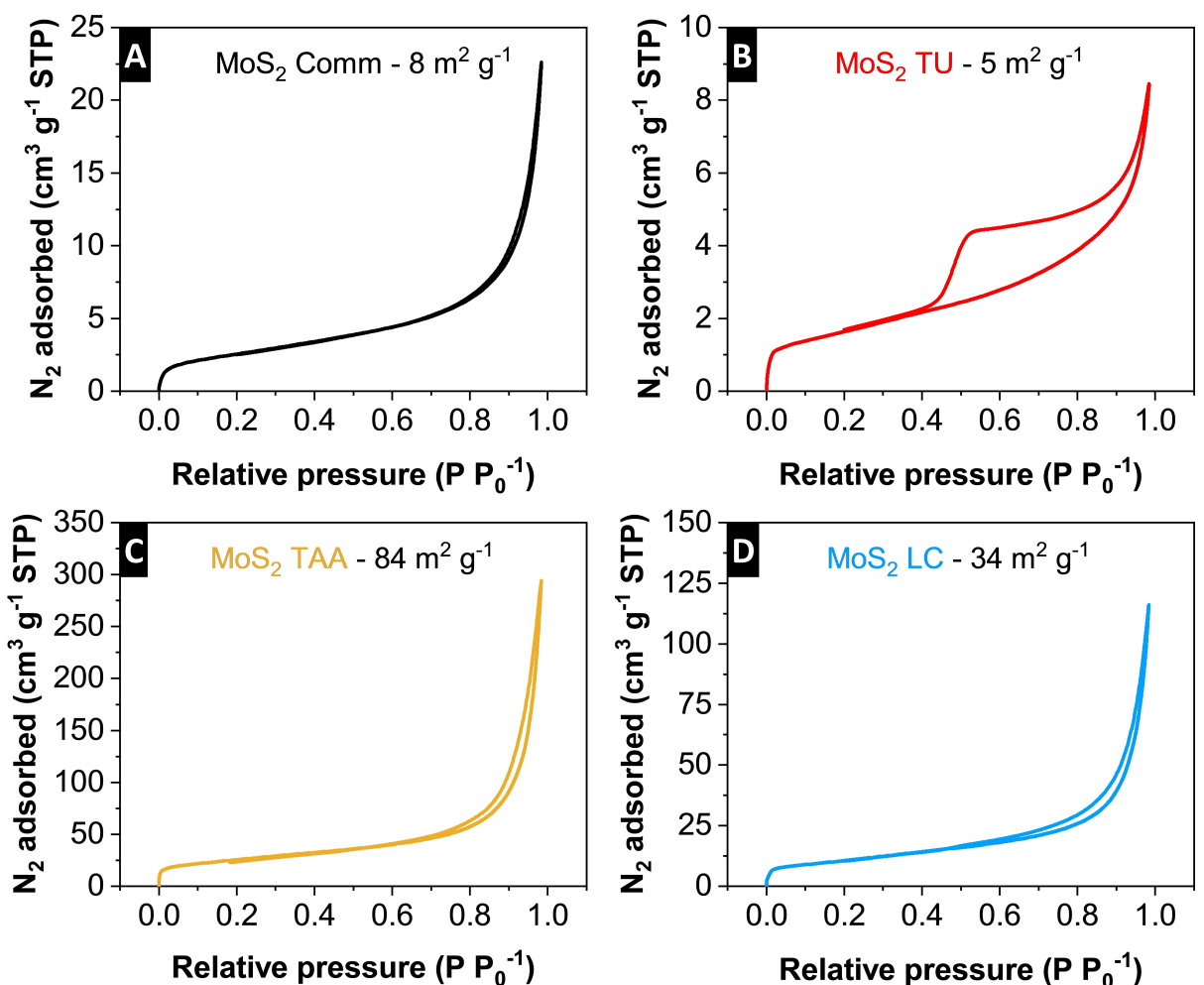


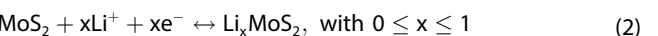
Figure 4. Nitrogen sorption isotherms at 77 K of MoS₂ based materials prepared from (A) Comm, (B) TU, (C) TAA, (D) LC.

Overall, structural investigation over several length scales demonstrates that the choice of sulfur precursor for hydrothermally synthesized MoS₂ has a large impact on the macroscopic secondary and primary particle morphology, the resulting sample porosity, as well as accessible surface area (TAA > LC > TU). On a microscopic level, however, crystallite size and lattice parameters remain comparable across the three samples.

Electrochemical Characterization

While it is demonstrated that the morphology, specific surface area and porosity of hydrothermally synthesized MoS₂ materials are strongly dependent on the utilized sulfur precursor, the samples show comparable, few-layer nano-crystallites with mixed 2H-/1T-phases. The materials therefore allow to study the impact of MoS₂ structural parameters on electrochemical lithium ion intercalation properties, allowing to draw conclusions on the preferred hydrothermal synthesis precursors and set the materials in relation to commercially available, pristine 2H-MoS₂ Comm.

Initial evaluation of electrochemical lithium intercalation behavior of MoS₂ electrode materials is conducted by galvanostatic charge/discharge technique between 3.0 to 1.0 V vs. Li/Li⁺, a potential range where reversible lithium intercalation into the MoS₂ interlayer space is expected according to:^[33]



The theoretical maximum capacity for the intercalation of 1 Li⁺ per MoS₂ is 167 mAh g⁻¹. Potential profiles of the first five galvanostatic cycles at a constant specific current of 20 mA g⁻¹ for each MoS₂ sample are presented in Figure 5A–D. MoS₂ Comm (Figure 5A) exhibits a plateau at ca. 1.1 V vs. Li/Li⁺ during first cycle associated with the irreversible phase transition from semi-conductive 2H phase to metallic 1T phase, resulting in an initial Coulombic efficiency (ICE) of 76%, well aligned to the literature values.^[17] It is a consequence of the sulfur plane gliding upon intercalation of lithium ions which turns the molybdenum atom into the octahedral coordination environment.^[34,35] In the consecutive few cycles, completion of the irreversible phase transition can still be observed, before a stable (de)lithiation profile with the main redox plateau in the

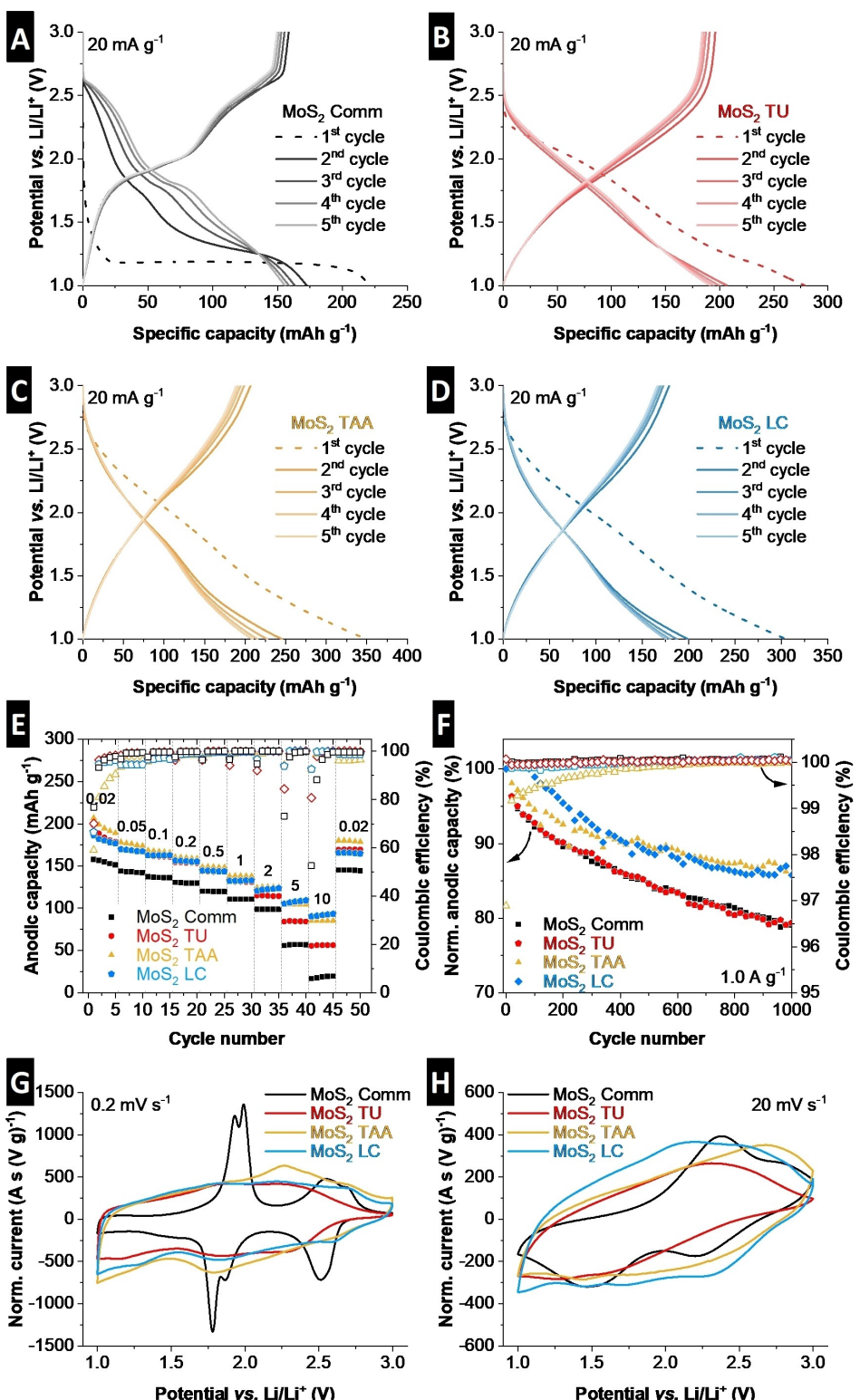


Figure 5. Electrochemical characterization of MoS_2 based materials. (A–D) First 5 cycles of galvanostatic charge/discharge profiles, (E) Anodic capacity recorded at different specific currents (from 20 mA g^{-1} to 10 A g^{-1}), (F) Galvanostatic charge/discharge stability at a specific current of 1 A g^{-1} , left y-axis indicate normalized anodic capacity (%), and right x-axis indicate Coulombic efficiency (%), (G–H) Cyclic voltammograms at 0.2 mVs^{-1} and 20 mVs^{-1} . All tests are carried out in coin cells versus lithium metal in LP30 electrolyte at a constant temperature of 20°C .

potential region around 1.7 – 1.9 V vs. Li/Li^+ is observed, presenting a reversible anodic/delithiation capacity of 152 mAh g^{-1} , close to the theoretical capacity. Comparable

behavior can be also observed when tested by cyclic voltammetry (Figure S1A), which shows high cathodic current peak

corresponding to phase transition in the first cycle and consequent de/intercalation behavior in the consecutive cycles.

The three samples prepared *via* hydrothermal synthesis (Figure 5B–D) exhibit linear/sloping galvanostatic profiles in absence of clear plateaus which are observed in MoS₂ Comm. The profiles electrically resemble capacitive-type charge storage processes that can be induced by nanosizing effects of the crystallites, leading to pseudocapacitive intercalation behavior. Thermodynamically, the effect can be explained by contributions of excess chemical potential of lithium at (near-)surface sites of MoS₂ nanocrystals dispersing the resulting redox potential.^[36,37] While the sloping potential profile of MoS₂ TU is observed between ca. 2.4–1.0 V vs. Li/Li⁺, the sloping potential region of MoS₂ TAA and MoS₂ LC is further expanded in the positive range to about 2.7 V. The pseudocapacitive intercalation behavior of the hydrothermally synthesized MoS₂ samples, especially in contrast to commercial MoS₂ Comm, can also be observed by cyclic voltammograms at various sweep rates between 0.2 mVs⁻¹ and 20 mVs⁻¹ (Figure 5G–H). The effect of scan rates for each material is presented in Figure S2.

Based on the peak current of the cyclic voltammograms as a function of scan rates, it is possible to further elucidate the charge storage kinetics by using b-value analysis (Figure S3–S4). B-values can be determined from the slope of the fitting curve of logarithmically plotted peak current versus scan rate, which allows for assessing whether the process of electrochemical ion intercalation is semi-infinite diffusion-controlled ($b=0.5$), finite diffusion-controlled ($b=0.6\text{--}0.8$) or surface-controlled ($b=1$).^[38] MoS₂ Comm reveals two redox peaks at 2 V and 2.5 V vs. Li/Li⁺ with b-values of 0.67 and 0.75 during the cathodic scan, correspondingly, which are indicative of (finite-length) diffusion-controlled charge storage. Contrary, hydrothermally prepared MoS₂ shows higher b-values, ranging from 0.82 (for MoS₂ TAA) to 0.99 (for MoS₂ LC), suggesting kinetically surface-controlled, pseudocapacitive intercalation.

In a comparison to MoS₂ Comm, hydrothermally synthesized MoS₂ materials do not show the pronounced plateau behavior of the 2H-to-1T phase transition at 1.1 V during first cycle, likely as a consequence of their high 1T phase content demonstrated by Raman. Only in MoS₂ TU it is visible to some extent. It can be also observed on the cyclic voltammograms during the first few cycles (Figure S1B–D). The ICEs of the samples are 70% for MoS₂ TU, 59% for MoS₂ TAA and 67% for MoS₂ LC, possibly caused by irreversible parasitic reactions at the electrode/electrolyte interface (considering lower ICE for samples with higher SSA) and remaining 2H-to-1T phase transition (specifically for MoS₂ TU). Each hydrothermally synthesized MoS₂ shows higher reversible (de)lithiation capacity than commercial MoS₂ Comm with around 200 mAh g⁻¹ (corresponds to ca. 1.2 Li⁺ per MoS₂), indicating additional charge storage for nanocrystalline MoS₂ materials. While this effect has been observed before for nanostructured MoS₂ and was attributed to additional surface redox reactions, it is remarkably also observed for MoS₂ TU with a SSA even smaller than that of commercial MoS₂ Comm, clearly demonstrating the significance of nano-crystallinity over accessible surface area for maximizing the reversible (de)lithiation capacity of MoS₂.^[16]

All MoS₂-based materials are galvanostatically cycled at different specific currents to investigate the rate capability of the (de)lithiation reaction (Figure 5E). As discussed above, hydrothermally synthesized MoS₂ samples exhibit higher anodic capacity than MoS₂ Comm over the entire range of specific currents. MoS₂ TAA and MoS₂ LC exhibit similar capacity as MoS₂ TU up to specific currents of around 1–2 Ag⁻¹, but at higher currents these samples show superior capacity retention (Figure S5). This is likely due to their higher specific surface area, leading to an increased electrode/electrolyte interface with reduced diffusion-limitations even at high rates due to smaller diffusion path lengths.^[13] The galvanostatic cycling stability is tested at an intermediate specific current rate of 1 Ag⁻¹ (Figure 5F). After 1,000 cycles, two groups can be identified according to their capacity retention. MoS₂ TAA and MoS₂ LC show comparably stable cycling behavior with about 86% of initial capacity retention, whereas MoS₂ Comm and MoS₂ TU only exhibit about 80% of capacity retention. Remarkably, this behavior is opposite to their increasing SSA, which is often hypothesized to be a source of capacity fading due to increased parasitic side reactions.^[39] It is demonstrated that MoS₂ materials with higher SSA exhibit improved cycling stability, regardless of crystallite size. We hypothesize that this behavior is a consequence of reduced volumetric electrode changes during cycling (*vide infra*). At the same time, MoS₂ TAA as the sample with the highest SSA (and therefore, the highest electrode/electrolyte interface), shows comparatively lower Coulombic efficiency over the first few hundreds of cycles (yet, still above 99%), which is likely caused by increased side reactions with the electrolyte.

To gain deeper insights into the kinetics of the MoS₂-based samples during lithium intercalation, electrochemical impedance spectroscopy (EIS) is carried out at various states of charge along the entire potential range from 3–1 V vs. Li/Li⁺ (Figure S6). The capacitor-like electrical response (i.e., pseudocapacitive or electrical double-layer contributions to the charge storage process) can be extracted from EIS by employing a simple equivalent circuit consisting of a capacitor and resistor in series.^[40] Then, the (pseudo)capacitive response can be presented over a wide potential range as a function of frequency *via* a so-called 3D Bode plot (Figure S7) with real capacitance representation (Figure 6).

For commercial MoS₂ Comm, two clear maxima of the real capacitance curve can be found corresponding to the two redox peak potentials (Figure 6A). Outside of these peak potentials, there is a significant drop in the real capacitance, in line with a typical battery-like electrochemical response like for example in LiFePO₄.^[24] Contrarily, for all three hydrothermally synthesized MoS₂ samples (Figure 6B–D), the real capacitance curve changes towards a “waterfall” shape indicating a (pseudo)capacitive charge storage process over a wider potential range. Notably, potential range is narrower for MoS₂ TU as compared to the other two samples, MoS₂ TAA and MoS₂ LC. Overall, 3D Bode analysis gives a comprehensive overview of electrode kinetics over a wide potential and frequency range, with pseudocapacitive lithium intercalation properties for hydrothermally synthesized MoS₂ samples.^[41]

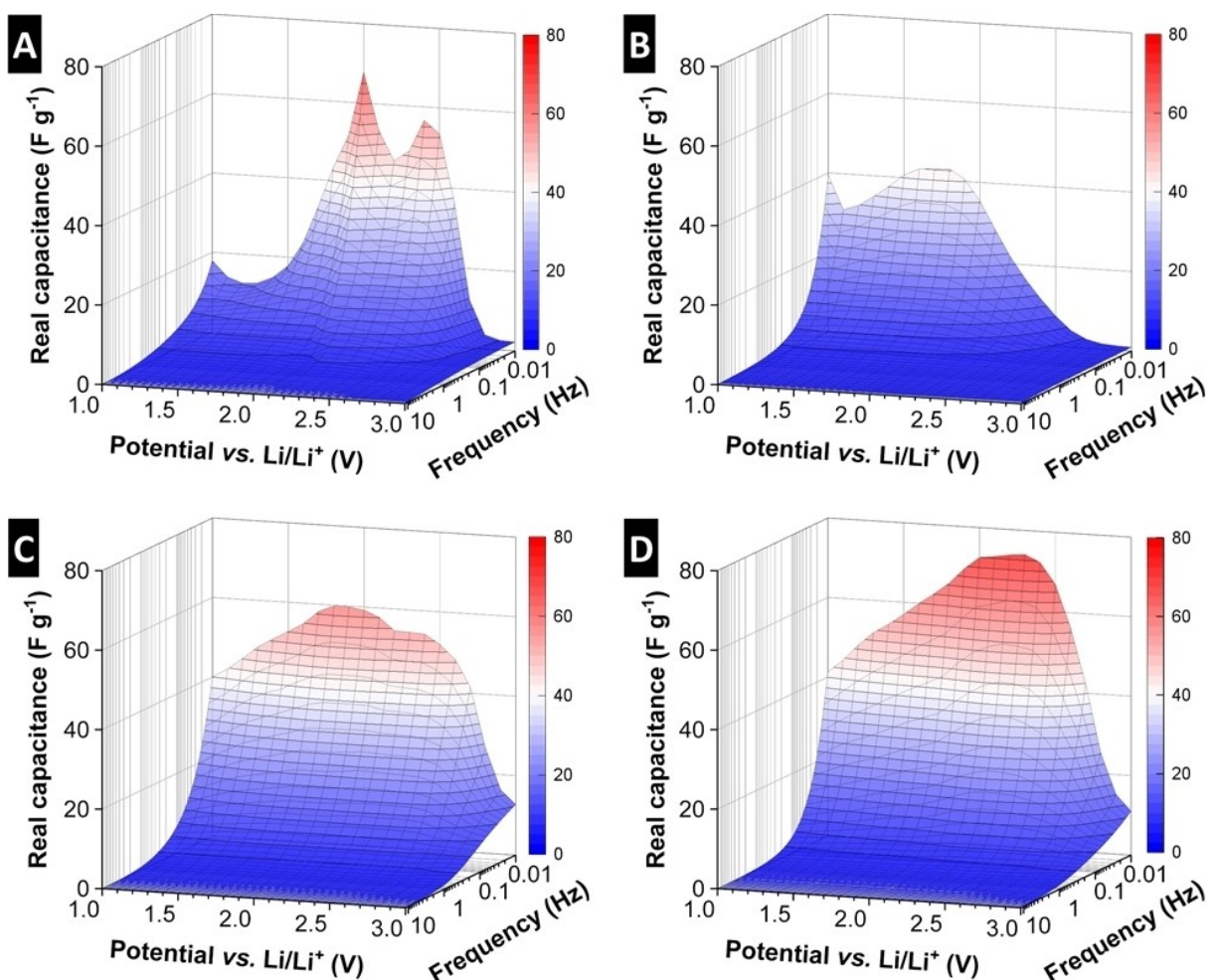


Figure 6. 3D Bode representation of real capacitance vs. frequency at different potentials during discharge for different MoS_2 materials (A) Comm, (B) TU, (C) TAA, (D) LC.

To better understand the origin of the different electrochemical response of the materials, operando XRD during the galvanostatic cycling is carried out to study the crystallographic changes during lithium (de)intercalation. MoS_2 Comm (Figure 7A) shows the initial (002) plane peak of 2H- MoS_2 , with a corresponding d-spacing of $d_{002}=0.61\text{ nm}$, decreasing in intensity during the discharge plateau at 1.1 V vs. Li/Li^+ , while another peak emerges at corresponding to the (001) plane of the 1T- MoS_2 phase ($d_{001}=0.63\text{ nm}$), in good agreement with the values reported in the literature for the 1T-Li MoS_2 phase.^[42] The subsequent deintercalation process appears as a solid-solution reaction, with the prominent (001) plane peak shifting to lower angles, corresponding to an expansion in the interlayer spacing ($d_{001}=0.65\text{ nm}$), followed by a contraction to $d_{001}=0.62\text{ nm}$ at the end of the deintercalation. The initial 2H- MoS_2 (002) peak is not recovered after the first cycle, which indicates an irreversible transformation from 2H- MoS_2 to 1T- MoS_2 , in close agreement with previous reports.^[17]

In MoS_2 TU (Figure 7B), the initial interlayer distance is 0.65 nm and only expands slightly to 0.67 nm upon lithiation. At the end of the first delithiation, the d-spacing remains at roughly 0.67 nm . The XRD signature is characterized by a

minimal, but continuous shifts of the (001) set of planes of 1T- MoS_2 , rather than the emergence of new diffraction signals, demonstrating solid-solution lithium (de)intercalation. While Raman results suggest that MoS_2 TU consists of a mixture of 1T- MoS_2 and 2H- MoS_2 , a phase transformation is not observed via operando XRD. This is likely due to the nanosizing effect of MoS_2 crystallites suppressing the transformation.^[14] Overall, crystallographic changes in MoS_2 TU are minimal during (de)lithiation, providing an explanation for the superior kinetics of the material compared to MoS_2 Comm, despite its small SSA. The operando XRD patterns of MoS_2 TAA and MoS_2 LC provide very little peak intensity during cycling, indicating a high degree of structural disorder, making interpretation of the results more challenging. While for MoS_2 TAA a continuous shift of the (001) plane of 1T- MoS_2 could be interpreted from the heatmap representation, somewhat comparable to MoS_2 TU, no clear signals can be observed for MoS_2 LC. However, the absence of any new XRD signals during cycling points towards a solid-solution intercalation process without the formation of a new phase for both samples. Thus, it can be summarized that in the case of hydrothermally synthesized MoS_2 , lithium

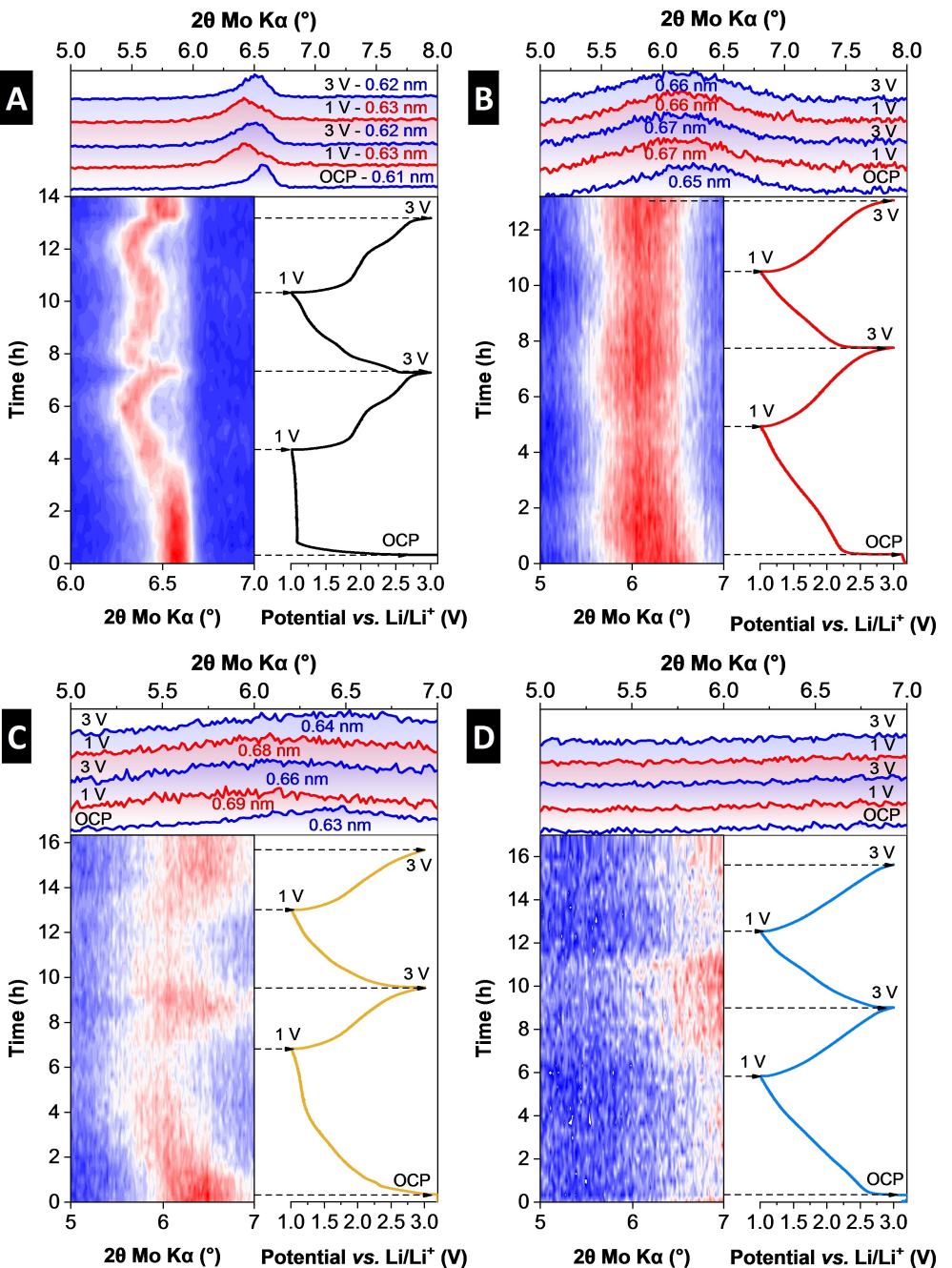


Figure 7. Operando XRD profiles for different MoS_2 -based materials: (A) MoS_2 Comm, (B) MoS_2 TU, (C) MoS_2 TAA, (D) MoS_2 LC. Measurements are carried out in Debye-Scherrer geometry using custom-designed coin cells with Kapton-taped holes allowing for X-ray penetration.

(de)intercalation proceeds via a solid-solution type mechanism regardless of the specific surface area of the samples.

To elucidate the volumetric changes in electrode materials on a macroscopic level, electrochemical dilatometry (ECD) is employed. The method is useful to investigate morphology/porosity-induced effects, which cannot be easily captured by methods like operando XRD. Thus, ECD is employed to compare the expansion/contraction behavior of MoS_2 Comm, the host material that undergoes a phase transformation during the first lithiation step, with MoS_2 LC which is the host material of the fastest kinetics that showed improved stability during long-

term cycling. For MoS_2 Comm (Figure 8A), a large increase in electrode thickness of about 19% can be observed during the irreversible phase transformation from 2H-to-1T. In subsequent cycles, contraction/expansion of about 2–3% can be observed during delithiation and lithiation, respectively. The initial irreversible thickness change is very significant and could not be explained by crystallographic expansion (using operando XRD), indicating that this expansion is potentially the consequence of significant solid electrolyte interphase (SEI) formation. Further work will more closely investigate the origin of the significant expansion behavior during the first lithiation cycle.

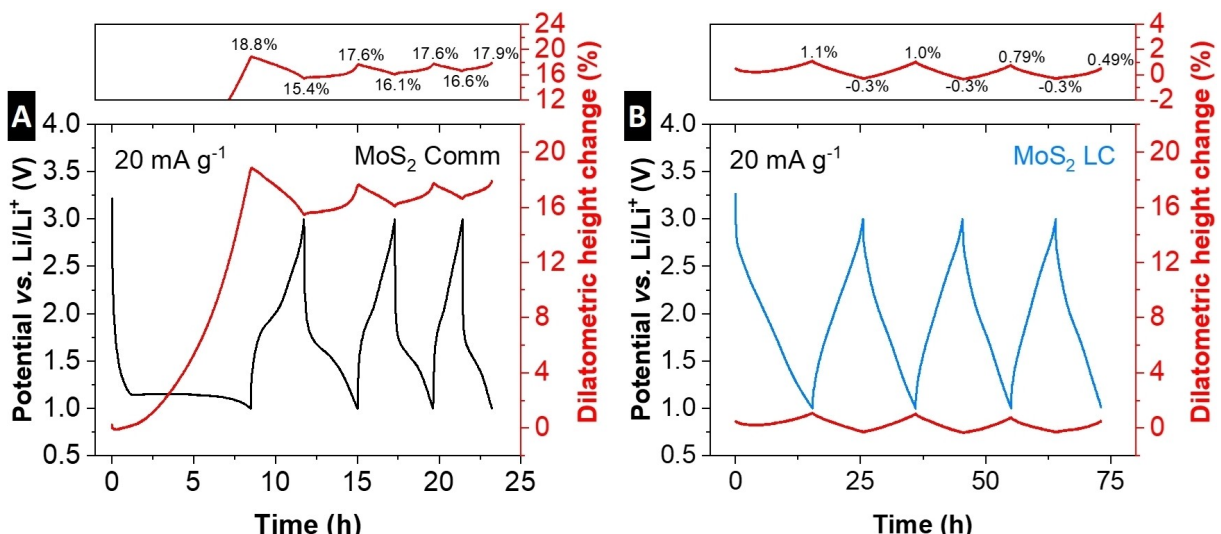


Figure 8. Dilatometric height change of the electrode materials over first few consecutive cycles. (A) MoS₂ Comm, (B) MoS₂ LC.

For MoS₂ LC, very minimal height changes are observed (Figure 8B). During the first lithiation process, the electrode expands by ca. 1 % and subsequently exhibits reversible height changes around 1 %. The significantly reduced height change of MoS₂ LC, especially during the first cycle, is a likely explanation for the improved cycling stability over MoS₂ Comm.

Conclusions

In this work, the choice of sulfur precursor is demonstrated as a facile route to control the structure and morphology of hydrothermally synthesized MoS₂ over several length scales. From a macroscopic point of view, morphology is affected by the precursor choice, with thiourea (MoS₂ TU) yielding micron-sized secondary particle architectures, whereas thioacetamide and L-cysteine provide reduced secondary particles with nano-sized, flake-like morphology (MoS₂ TAA and MoS₂ LC). Further, the resulting sample porosity and (accessible) surface area follows the same trend (TAA>LC>TU). Contrarily, on a microscopic level, crystallite size and lattice parameters remain comparable across all three samples demonstrating nanoscopic crystalline domains with a mixture of 2H- and 1T-phases.

When employed as a host material for electrochemical lithium intercalation, each material shows fast pseudocapacitive charge storage behavior with slightly different electrochemical response showing strong correlation to the available adsorption area and particle size of the crystalline domains explained by 3D bode plot analysis. Each hydrothermally prepared sample shows higher maximum anodic capacity of ca. 200 mAh g⁻¹ at a rate of 20 mA g⁻¹ in comparison to commercially available MoS₂ with 152 mAh g⁻¹. MoS₂ TAA and MoS₂ LC demonstrate significantly improved rate capability, with higher charge retention at 10 Ag⁻¹ (related to ca. 34 s discharge) up to 90 mAh g⁻¹ in comparison to MoS₂ TU (50 mAh g⁻¹) and MoS₂ Comm (25 mAh g⁻¹). Long term cycling reveals that the samples

with high specific surface area and small secondary particle size show slightly better stability over 1,000 cycles, possibly due to smaller volumetric expansion of the electrode material during the first cycles revealed during dilatometric studies.

The study demonstrates the ability to influence electrochemical charge storage properties of MoS₂ by the choice of hydrothermal precursor, offering a facile strategy to control materials structure and functionality. Such insights can be useful for researchers in the field of high-power electrochemical energy storage materials, but can also be of value to materials developed in other fields of electrochemistry such as electrocatalytic hydrogen evolution and beyond.

Acknowledgements

M.T. and E.F. acknowledge financial support from National Science Centre, Poland within the project Preludium 20 2021/41/N/ST5/01364 and Polish National Agency for Academic Exchange (NAWA) under STER programme, Towards Internationalization of Poznan University of Technology Doctoral School (2022–2024). M.E., J.C., and S.F. acknowledge funding from the German Federal Ministry of Education and Research (BMBF) in the NanoMatFutur program (grant No. 03XP0423). S.F. would like to thank the Daimler and Benz Foundation for financial support in the Scholarship program. The authors are thankful for basic funding from the Helmholtz Association. Open Access funding enabled and organized by Projekt DEAL.

Conflict of Interests

There are no conflicts of interest to declare.

Data Availability Statement

The data that support the findings of this study are available from the corresponding author upon reasonable request.

Keywords: molybdenum disulfide • hydrothermal synthesis • sulfide precursor • pseudocapacitance • electrochemical dilatometry

- [1] A. V. Kolobov, J. Tominaga, *Two-Dimensional Transition-Metal Dichalcogenides*, Springer Series in Materials Science, vol 239. Springer, Cham 2016, p. 7–27.
- [2] M. A. Bissett, S. D. Worrall, I. A. Kinloch, R. A. W. Dryfe, *Electrochim. Acta* 2016 201, 30–37.
- [3] M. Acerce, D. Voiry, M. Chhowalla, *Nat. Nanotechnol.* 2015 10, 313–318.
- [4] C. Tsai, F. Abild-Pedersen, J. K. Nørskov, *Nano Lett.* 2014, 14, 1381–1387.
- [5] J. Zhu, Z. C. Wang, H. Dai, Q. Wang, R. Yang, H. Yu, M. Liao, J. Zhang, W. Chen, Z. Wei, N. Li, L. Du, D. Shi, W. Wang, L. Zhang, Y. Jiang, G. Zhang, *Nat. Commun.* 2019, 10, 1348–1348.
- [6] M. Chhowalla, H. S. Shin, G. Eda, L. J. Li, K. P. Loh, H. Zhang, *Nat. Chem.* 2013, 5, 263–275.
- [7] R. Lv, J. A. Robinson, R. E. Schaak, D. Sun, Y. Sun, T. E. Mallouk, M. Terrones, *Acc. Chem. Res.* 2015, 48, 56.
- [8] M. Zeng, Y. Xiao, J. Liu, K. Yang, L. Fu, *Chem. Rev.* 2018, 118, 6236–6296.
- [9] T. Stephenson, Z. Li, B. Olsen, D. Mitlin, *Energy Environ. Sci.* 2014, 7, 209–231.
- [10] G. Wang, J. Zhang, S. Yang, F. Wang, X. Zhuang, K. Müllen, X. Feng, *Adv. Energy Mater.* 2018, 8, 1–8.
- [11] C. George, A. J. Morris, M. H. Modarres, M. De Volder, *Chem. Mater.* 2016, 28, 7304–7310.
- [12] H. D. Yoo, Y. Li, Y. Liang, Y. Lan, F. Wang, Y. Yao, *ChemNanoMat* 2016, 2, 688–691.
- [13] J. B. Cook, H. S. Kim, T. C. Lin, C. H. Lai, B. Dunn, S. H. Tolbert, *Adv. Energy Mater.* 2017, 7, 1–12.
- [14] J. B. Cook, T. C. Lin, H.-S. Kim, A. Siordia, B. S. Dunn, S. H. Tolbert, *ACS Nano* 2019, 13, 1223–1231.
- [15] J. Choi, H. Moon, S. Fleischmann, *Electrochim. Acta* 2024, 476, 143774.
- [16] Y. Yao, H. Cumberbatch, D. D. Robertson, M. A. Chin, R. Lamkin, S. H. Tolbert, *Adv. Funct. Mater.* 2023, 2304896.
- [17] X. Fang, C. Hua, X. Guo, Y. Hu, Z. Wang, X. Gao, F. Wu, J. Wang, L. Chen, *Electrochim. Acta* 2012, 81, 155–160.
- [18] L. Zhou, T. Xia, T. Cao, L. Wang, Y. Chen, S. Li, R. Wang, H. Guo, *J. Alloys Compd.* 2020, 818, 152909.
- [19] Z. Ali, Q. Hussain, M. A. Yawer, M. Mahmood, R. Hussain, A. Shah, H. Kanwal, A. Yawer, S. Ahmad, S. Zahid, *J. Mol. Struct.* 2023, 1278, 134929.
- [20] X. Zheng, Y. Zhu, Y. Sun, Q. Jiao, *J. Power Sources* 2018, 395, 318–327.
- [21] Y. Liu, K. Wu, X.-I. Guo, W.-y. Wang, Y.-q. Yang, *J. Fuel Chem. Technol.* 2018, 46, 535–542.
- [22] I. S. Waskito, B. Kurniawan, M. I. Amal, M. Hanifuddin, *Mater. Sci. Eng.* 2019, 546, 042048.
- [23] J. Liu, J. Wang, B. Wei, Y. Xue, L. Ma, R. Jiang, *Inorg. Chem.* 2023, 62, 9749–9757.
- [24] J. S. Ko, C.-H. Lai, J. W. Long, D. R. Rolison, B. Dunn, J. Nelson Weker, *ACS Appl. Mater. Interfaces* 2020, 12, 14071–14078.
- [25] K. Chang, W. Chen, *ACS Nano* 2011, 5, 4720–4728.
- [26] S. Guo, Y. Zhang, S. Tang, B. Wang, Y. Wang, Y. Song, X. Xin, Y. Zhang, X. Li, *J. Alloys Compd.* 2011, 864, 158581.
- [27] H. Li, Q. Zhang, C. C. R. Yap, B. K. Tay, T. H. T. Edwin, A. Olivier, D. Baillargeat, *Adv. Funct. Mater.* 2012, 22, 1385–1390.
- [28] C. Lee, H. Yan, L. E. Brus, T. F. Heinz, J. Hone, S. Ryu, *ACS Nano* 2010, 4, 2695–2700.
- [29] X. Zang, Y. Qin, T. Wang, F. Li, Q. Shao, N. Cao, *ACS Appl. Mater. Interfaces* 2020, 12, 55884–55893.
- [30] X. Geng, Y. Zhang, Y. Han, J. Li, L. Yang, M. Benamara, L. Chen, H. Zhu, *Nano Lett.* 2017, 17, 1825–1832.
- [31] M. Thommes, K. Kaneko, A. V. Neimark, J. P. Olivier, F. Rodriguez-Reinoso, J. Rouquerol, K. S. W. Sing, *Pure Appl. Chem.* 2015, 87, 1051–1069.
- [32] S. Brunauer, P. H. Emmett, E. Teller, *J. Am. Chem. Soc.* 1938, 60, 309–319.
- [33] T. Wang, S. Chen, H. Pang, H. Xue, Y. Yu, *Adv. Sci.* 2017, 4, 1600289.
- [34] F. Wypych, R. Schollhorn, *J. Chem. Soc.* 1992, 1386–1388.
- [35] Q. Jin, N. Liu, B. Chen, D. Mei, *J. Phys. Chem. C* 2018, 122, 28215–28224.
- [36] J. Maier, *J. Power Sources* 2007, 174, 569–574.
- [37] J. Nanda, V. Augustyn, *Nanostructured Transition Metal Oxides for Electrochemical Energy Storage*, John Wiley & Sons 2022, pp. 183–212.
- [38] J. Wang, J. Polleux, J. Lim, B. Dunn, *J. Phys. Chem. C* 2007, 111, 14925–14931.
- [39] E. Pomerantseva, Y. Gogotsi, *Nat. Energy* 2017, 2, 17089.
- [40] P. L. Taberna, P. Simon, J. F. Fauvarque, *J. Electrochem. Soc.* 2003, 150, A292–A300.
- [41] R. Holze in *Electrochemical Methods. Fundamentals and Applications*, 2nd Edition (Eds: A. J. Bard, L. R. Faulkner), Angewandte Chemie International, 2002, 41, pp. 655–657.
- [42] M. A. Py, R. R. Haering, *Can. J. Phys.* 1983, 61, 76–84.

Manuscript received: April 23, 2024

Revised manuscript received: June 6, 2024

Accepted manuscript online: July 2, 2024

Version of record online: August 20, 2024